Exploring N6-Methyladenosine and long transcripts in glioma cells and extracellular vesicles.

Syeda Maheen Batool[1*], Ana K. Escobedo[1*], Hanna Lee[1], Prerna Khanna[1], Kase D. Haas[1], Tiffaney Hsia[1], Bob S. Carter[1], Leonora Balaj[1]

[1]Department of Neurosurgery, Massachusetts General Hospital, Harvard Medical School, Boston, MA, USA
[*] co-first authors

Corresponding author: Email: Balaj.leonora@mgh.harvard.edu Adresss:185 Cambridge St. Boston, MA 02114

Abstract

Glioma represents the most common primary central nervous system (CNS) neoplasm in adults. Previous studies have identified m^6A as a key player in glioma pathogenesis, promoting cell stemness and tumor cell proliferation. However, there is also evidence of a potential anti-cancer role of m^6A. Here, we present a comprehensive overview of the m^6A landscape in a glioma cell line model using Nanopore direct RNA sequencing platform. The study investigates functional and biological impact of targeted knockdown (KD) of key m^6A regulators (reader: IGF2BP2, writer: METTL3, eraser: ALKBH5). Transcriptome wide mapping of m^6A demonstrated enrichment in CDS and 3'UTR regions. Differential patterns of non-DRACH motifs were observed across the KD conditions. Our analysis identified 716 common m^6A sites across all conditions and clusters of KD specific modifications enriched for distinct functional pathways. IGF2BP2 KD was associated with pathways involving protein metabolism and apoptosis regulation. METTL3 KD was linked to cell cycle and stress response regulation and ALKBH5 KD impacted ribosome biogenesis and protein synthesis. Here, for the first time we also report detection of full-length RNA transcripts in extracellular vesicles (EVs) derived RNA from knockdown and control conditions. These findings underscore the unique contributions of each m^6A regulator to glioma cell transcriptomics and suggest potential pathways for elucidating the overall role of m^6A machinery in glioma pathogenesis. Important clinical applications include identification of novel diagnostic, prognostic, and therapeutic m^6A RNA biomarkers.

Introduction

There are over 163 characterized RNA modifications, with methylation of adenosine at position N6, (m^6A) identified as one of the most prevalent modification in different types of RNAs (mRNA, tRNA, rRNA, circRNA, miRNA, lncRNA)[1,2]. Three distinct groups of binding proteins, widely known as "m^6A regulators" work together to maintain a dynamic balance of m^6A RNA expression: m^6A-binding proteins, or readers; detect base alteration, methyltransferases, or writers; catalyze or deposit, and demethylases, or erasers; remove the alteration[3,4]. The regulatory role of m^6A has been described in relation to but not limited to RNA translation, alternative splicing, intra- and extra-cellular transport, localization, and post-transcriptional stability[5].

Previous studies have generated considerable evidence identifying the biological role of m^6A RNA methylation in both physiological and pathological progressions of hematopoietic, central nervous and reproductive systems[3]. Emerging evidence indicates a higher prevalence of m^6A in CNS (central nervous system) relative to other organs[6]. Glioma is the most common primary CNS tumor and Glioblastoma (GBM) represents the most aggressive subtype[7]. Tumor recurrence and treatment resistance account for the poor prognosis of these heterogeneous lesions with a median survival of approximately 15 months[8,9]. An understanding of underlying molecular pathogenic mechanisms is crucial to advancing the development of earlier diagnosis and inclusion of targeted therapeutics.

m^6A has been previously identified as a key player in glioma progression[10]. Several mechanisms of gliomagenesis have been proposed including, enhancement of cell stemness[11,12], tumor cell proliferation[12], and modulation of the tumor microenvironment[13]. However, studies have also demonstrated anticancer properties of m^6A regulators, with lower m^6A levels promoting tumorigenesis of glioma stem cells (GSCs)[14]. The findings are suggestive of a potential dual role of m^6A in glioma progression and suppression necessitate a thorough and comprehensive exploration of the m^6A landscape in gliomas.

Our study aims to decipher the precise role of varying m^6A levels in a glioma cell line (Gli36) model. Herein, we present a workflow that generates knockdown (KD) models for an *in-vitro* analysis of the functional and biological consequences of key m^6A regulators: IGF2BP2 KD (reader), METTL3 KD (writer), and ALKBH5 KD (eraser). Using Oxford Nanopore technologies (ONT), we mapped the m^6A in isolated RNA at a single nucleotide resolution level. Each sample was sequenced in three independent runs. The findings represent an important step to advancing the understanding of m^6A RNA modifications in the context of gliomas.

Results

A.

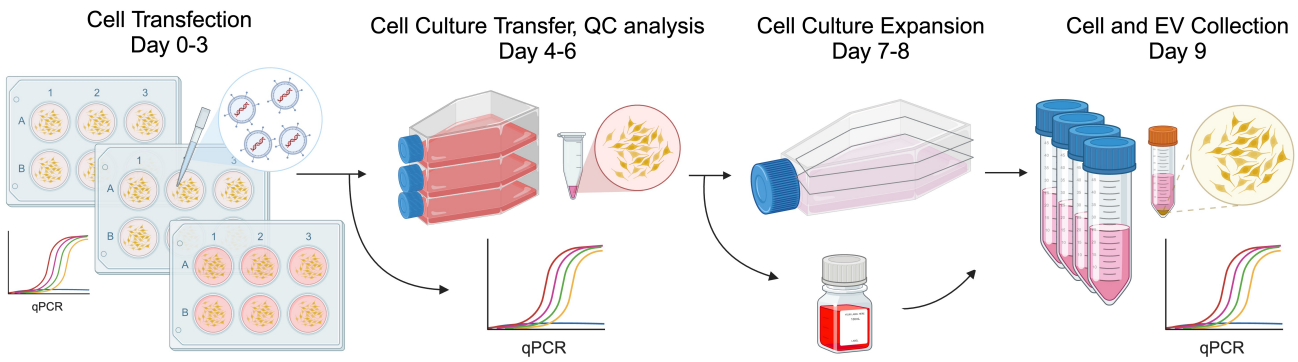

B.

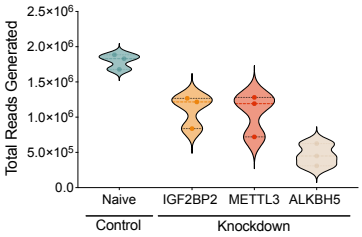

C.

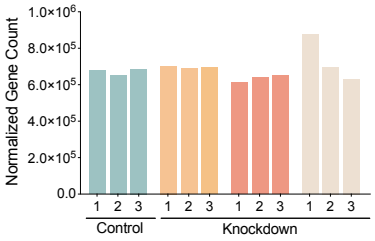

D.

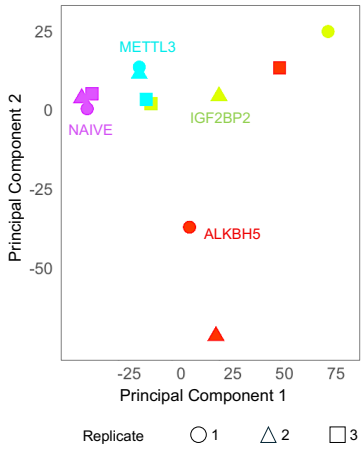

E.

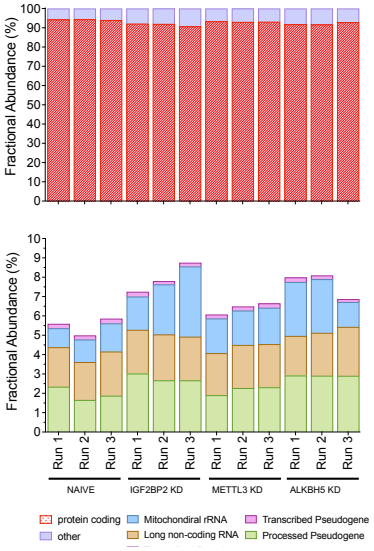

F.

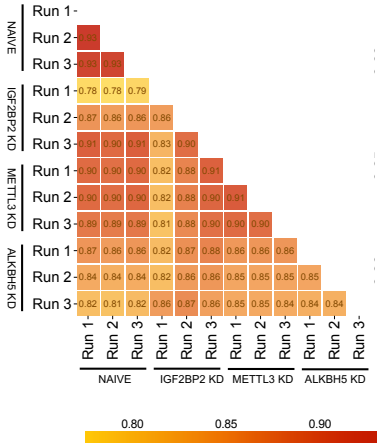

G.

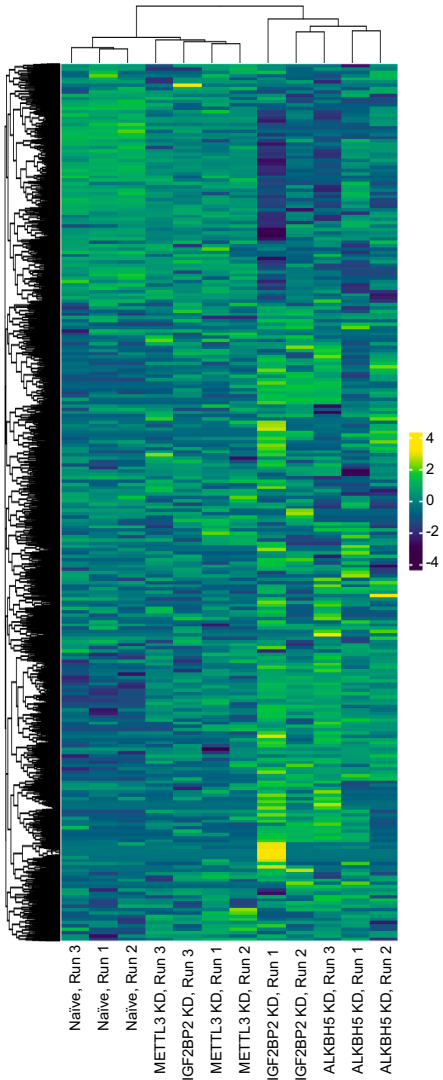

Figure 1. Transcriptome wide profiling m^{6}A in glioma cell line. *(a) Schematic depicting cell transfection with silencer RNA (siRNA) to achieve knockdown (KD) of key m^{6}A regulators: IGF2BP2 (reader), METTL3 (writer), ALKBH5 (eraser). RNA isolated from control and KD cells and extracellular vesicles (EVs) on day 9 sequenced using Nanopore direct RNA sequencing platform. Three technical replicates sequenced per condition. (b) Total and (c) Normalized (variance-stabilizing transformation, VST) gene counts detected across the three replicates of cell RNA sequenced from control and KD conditions. (d) Assessment of variance in the cell RNA detected transcripts using principal component analysis (PCA). (e) Distribution analysis of the detected RNA biotypes from control and KD conditions. (f) Pearson correlation analysis of individual sequencing runs. (g) Heatmap depicting clustering analysis of the detected transcripts demonstrating change in expression patterns across the control and knockdown conditions.*

Mapping of full length transcripts in cell RNA.

Glioma cell line (Gli36, EGFRvIII mutant) was transfected with silencer RNA (siRNA) to induce knockdown of selected m^{6}A regulators: IGF2BP2 (reader), METTL3 (writer), and ALKBH5 (eraser) (**Fig. 1a**). Total RNA from transfected (knockdown) and naive (untreated, control) cells and extracellular vesicles (EVs) was sequenced using Oxford Nanopore Technologies (ONT) direct RNA sequencing platform (**see Methods**). Three replicates were sequenced per condition.

Preliminary analysis of the sequencing output from cells demonstrated an overall higher number of reads generated in naive vs. knockdown conditions (**Fig. 1b**). Variance stabilizing transformation (VST) was performed to normalize the gene counts across the naive and knockdown conditions (**Fig. 1c**). Results from principal component analysis (PCA) (**Fig. 1d**) demonstrated an overall 37.2% total variance in the data, with PC1 accounting for 24.8% of the variance, and PC2 contributing 12.4%. Finally, correlation assessment per condition yielded consistency of the transcripts detected across the three replicates (**Fig. 1f**).

Relative abundance of the RNA biotypes demonstrated no significant differences in the prevalence of protein coding RNA across naive and knockdown conditions (**Fig. 1e, top**). In the non-protein coding biotypes (**Fig. 1e, bottom**), we noted a higher prevalence of mitochondrial rRNA in IGF2BP2 KD (2.64%) and ALKBH5 KD (2.28%) cell RNA vs. METTL3 KD (1.82%) and naive cell RNA (1.20%) (**Fig. 1e, bottom**). Both transcribed and processed pseudogenes were similarly distributed across the conditions (**Fig. 1e, bottom**).

Clustering of the transcripts detected (normalized, VST) highlighted the distinct expression in the knockdown conditions vs. naive (**Fig. 1g**). Furthermore, ALKBH5 KD RNA demonstrated the most remarkable change in the pattern of transcript expression when compared to Naive condition (**Fig. 1g**).

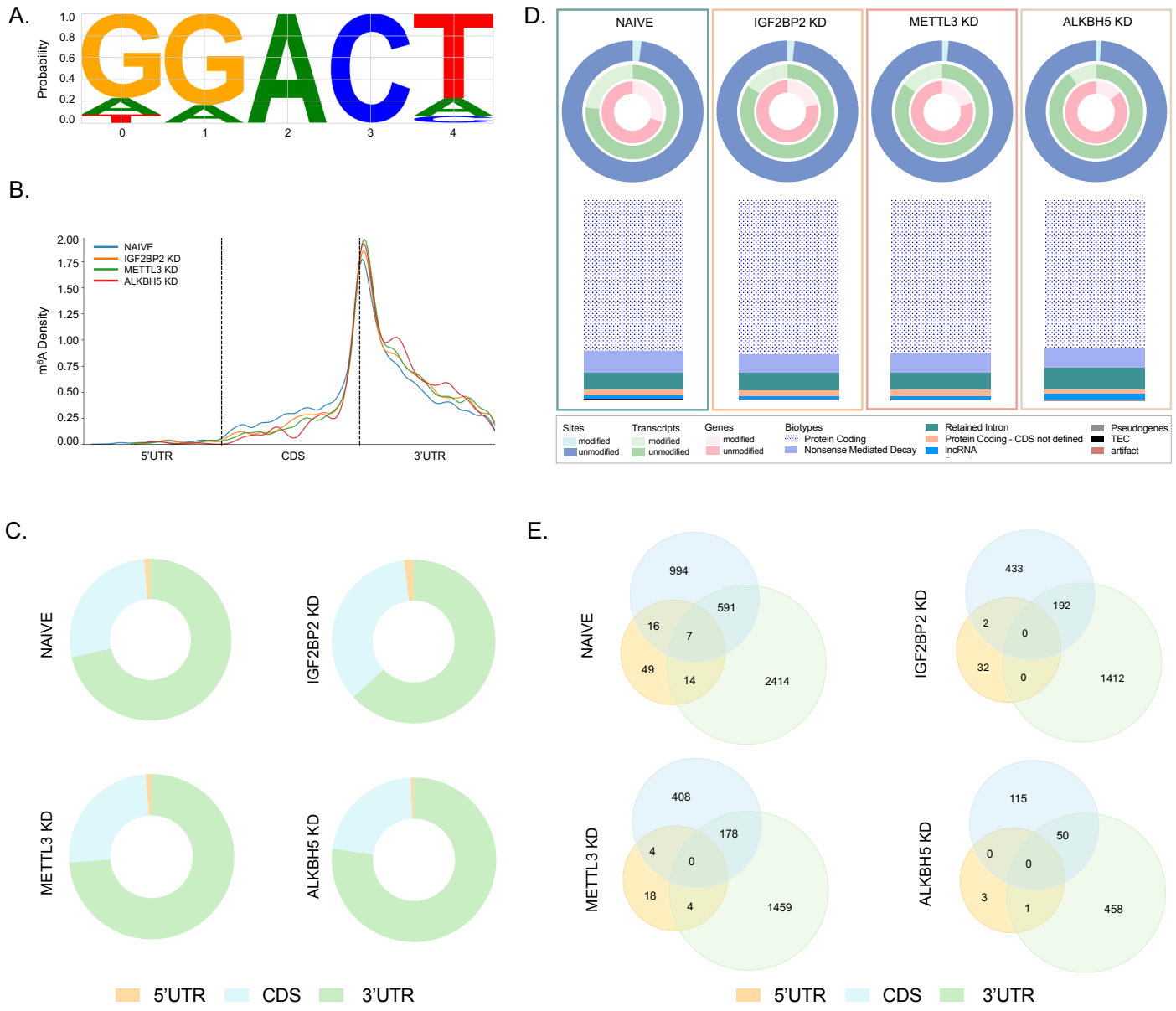

Figure 2. Deduction of m^{6}A consensus motifs and transcriptome wide distribution and biotype analysis of m^{6}A modifications. *(a) Consensus MOTIF definition of m^{6}A modifications detected in the transcriptome of glioma cell line. Bitplot depicting the nucleotide composition with height of each symbol indicating the relative frequency of each nucleotide at that position. (b) Metagenes plot depicting m^{6}A RNA mapping in a transcriptome pattern across the naïve and knockdown conditions. (c) Pie charts depicting the relative distribution (%) of unique transcripts modified across the transcript regions in naïve and knockdown conditions. (d, top) Pie charts summarizing the prevalence of modified vs. unmodified m^{6}A sites (blue), transcripts (green), and genes (pink). (d, bottom) Stacked plots depicting the*

biotype distribution of m^6A RNA transcripts in naïve and knockdown conditions. (e) Venn diagrams quantifying single vs. multi region m^6A methylated RNA transcripts.

Mapping of m^6A sites across transcripts in cell RNA.

In our analysis of cell line derived m^6A modified RNA, we identified a significant number of m^6A motifs (probability score ≥ 0.9), categorized into DRACH (D = A/G/U, R = A/G, A = m^6A, C = C) motifs (**Fig. 2a**). No differences were observed in the nucleotide composition and probability distribution of the DRACH motifs in naive vs. knockdown conditions (**Supplementary Figure 1**). Overall, the DRACH motif, characterized by the sequence DRA*CH (where * denotes m^6A site), demonstrated a high probability of occurrence for the nucleotides 'G' at positions 1 and 2, 'A' at positions 3, 'C' at position 4, and 'T' at position 5 (**Fig. 2a**). This motif is consistent with the canonical DRACH sequence known to be enriched in m^6A sites. Transcriptome wide profiling of detected m^6A sites demonstrated an enrichment at the junction of CDS and 3'UTR region (near the stop codon) and the 3'UTR region. This pattern was noted in all conditions with no treatment specific regional differences noted (**Fig. 2b**).

Next, we performed a quantitative analysis of the m^6A sites sorted by transcript regions (**Fig. 2c**). When comparing 5'UTR region, the lowest enrichment of m^6A sites was seen in ALKBH5 KD (0.70%) vs. naive (1.31%) and other knockdown conditions (IGF2BP2 KD: 1.92%, METTL3 KD: 1.14%). ALKBH5 KD RNA also had the least detected m^6A sites in the CDS region (22.16%) while IGF2BP2 KD RNA had the highest prevalence of m^6A sites (34.96%) (**Fig. 2c**). Considerable variation was seen in the m^6A sites detection in 3'UTR region when comparing naive (71.48%) vs. knockdown conditions. While METTL3 KD RNA had a similar abundance (73.87%) as naive, lower abundance was seen in IGF2BP2 KD (63.12%) and higher abundance in ALKBH5 KD (77.15%) (**Fig. 2c**). We then extended the comparison to investigate the regional (5'UTR, CDS, 3'UTR) distribution of m^6A sites in the unique transcripts detected across all conditions (**Fig. 2e**). A total of n = 7 transcripts were shown to be methylated in all three regions in the naive condition. However, no transcripts with this pattern of modification were seen in the knockdown conditions (**Fig. 2e**). Finally, consistent with previous findings, all conditions had a significant proportion of transcripts modified in both CDS and 3'UTR regions (**Fig. 2e**).

Overall, of all the sites detected a greater proportion of unmodified vs. modified sites seen in all conditions (**Fig. 2d, top**). Highest prevalence of modified transcripts was seen in naive condition (23.41%) followed by IGF2BP2 KD (15.86%), METTL3 KD (15.07%), and ALKBH5 KD (9.78%) (**Fig. 2d, top**). Similar distribution was also seen at the gene level with highest prevalence of modified genes in naive (30.02%) and lowest prevalence in ALKBH5 KD (13.64%) (**Fig. 2d, top**). Stratification of the detected m^6A modified transcripts by biotypes yielded around 76% modified protein coding transcripts in both IGF2BP2 and METTL3 KD conditions (**Fig. 2d, bottom**). ALKBH5 KD condition yielded lowest abundance of protein coding (73.97%) transcripts but, highest prevalence of modified lncRNA (2.78%) transcripts when compared to naive (1.88%), IGF2BP2

KD (1.42%), and METTL3 KD conditions (1.79%). No significant differences were noted in distribution of other (Nonsense mediated decay, retained intron, pseudogenes) biotypes (**Fig. 2d, bottom**).

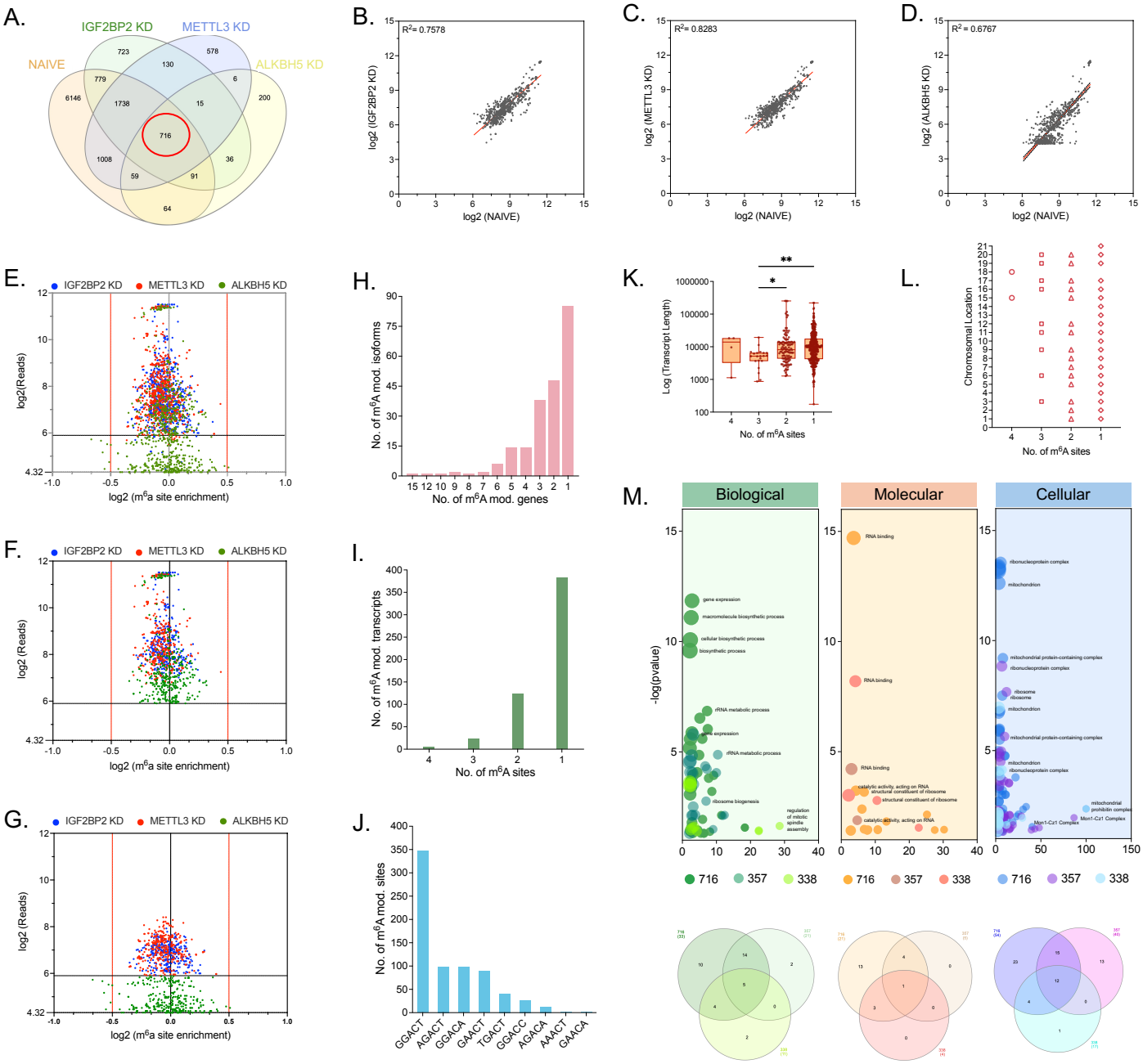

Figure 3. Overview of the detected m6A landscape in glioma cell line model. *(a) Venn diagram demonstrating the overlap of detected m6A sites in naive (control) and knockdown (IGF2BP2 KD, METTL3 KD, ALKBH5 KD) conditions. N = 716 sites detected in all conditions circled in red. (b-d) Pearson correlation analysis of enrichment of the common (n = 716) m6A sites in knockdown vs. naive condition. XY graphs plotting log2 reads, naive vs. log2, reads*

KD in: (b) IGF2BP2 KD, (c) METTL3 KD, (d) ALKBH5 KD. (e-g) Scatter plots demonstrating the distribution of the n = 716 sites across all conditions. For each site log2 (reads, y-axis) plotted against log2 (m6A site enrichment) with the color of the dot denoting the knockdown condition. Three clusters visualized: (e) n = 716 sites, (f) n = 357 sites, log2 (reads) > 5.9, (g) n = 338 sites, log2 (reads) > 5.9 present only in IGF2BP2 KD and METTL3 KD conditions. (h-j) Bar-graphs quantifying key parameters of the detected n = 716 m6A sites: (h) frequency of m6A modification per gene, (i) frequency of m6A modification per transcript, (j) frequency of detected m6A kmers. (k) Scatter-plot comparing the transcript length distribution in transcripts with 1 vs. > 1 m6A sites. (l) Dot-plot summarizing the chromosomal distribution of n = 716 m6A sites. (m) Gene ontology (GO) analysis of the three clusters of detected m6A sites (716, 357, 338) using ShinyGO. Multiple variable graphs plotting fold enrichment and –Log (p-value) of the enriched pathways in: biological process (green), molecular function (orange), and cellular compartment (blue). Venn diagrams quantifying the number of shared and unique pathways across the three clusters.

Common m^{6}A sites detected in all conditions.

Prior to investigation of knockdown specific m^{6}A sites, we performed a quantitative analysis of the n = 716 m^{6}A sites detected in naive and all three knockdown conditions (**Fig. 3a**). To remove bias secondary to variation in sequencing coverage, correlative analysis of the expression levels of each site was performed in the knockdown (IGF2BP2, METTL3, ALKBH5) vs. naive condition (**Fig. 3c-d)**. Overall, the results indicated similar detection levels of the 716 m^{6}A sites, with the highest strength of correlation seen in METTL3 KD (**Fig. 3c**; R^2, 0.83) followed by IGF2BP2 KD (**Fig. 3b**; R^2, 0.76) and ALKBH5 KD (**Fig. 3d**; R^2, 0.68). Next, level of m^{6}A enrichment at each site was computed using the predicted m^{6}A modification ratio (mod ratio) as follows: log2 (m^{6}A mod ratio, knockdown/m^{6}A mod ratio, naive) (**Fig. 3e-g)**. The calculated fold change demonstrated similar m^{6}A enrichment of the 716 sites in the knockdown vs. naive condition (**Fig. 3e**). Further sub-clustering of the 716 m^{6}A sites was done by setting a cut-off of log2 reads > 5.9 (**Fig. 3f-g**). Using this threshold we were able to further stratify the 716 sites into two clusters: 357 sites present in all knockdown conditions (**Fig. 3f**), and 338 sites detected only in IGF2BP2 KD and METTL3 KD conditions (**Fig. 3g**). Of the detected 716 m^{6}A sites, the majority (n = 85) of the genes had only one modified isoform and n = 28 genes had > 4 modified isoforms (**Fig. 3h**). Interestingly, the gene with the highest number of modified isoforms (n = 15) was shown to be EEF1A1 (**Fig. 3h**). At the individual transcript level, we saw a similar distribution with the majority of the transcripts (n = 383) being methylated at a singular site (**Fig. 3i**). Of the multi-methylated (> 1 m^{6}A site) transcripts, a total of 4 transcripts had 4 m^{6}A sites each (**Fig. 3i**). Furthermore, as seen previously, the DRACH motif was the most common kmer present in the 716 m^{6}A sites followed by similar counts of AGACT (n = 99), GGACA (n = 98), and GAACT (n = 89) (**Fig. 3j**). To further study the differences in RNA transcript structure leading to singular vs. multiple m^{6}A sites, we compared the transcript lengths sorted by the number of m^{6}A sites (1-4, **Fig. 3k**). Overall, significantly higher variation was seen in transcripts with n = 1 (range 219,586 bp; 174-219,760 bp) and n = 2 (range 250,379 bp; 1,266-

251,645 bp) m^6A sites vs. transcripts with n = 3 (range 18,400 bp; 870-19,270 bp) and n = 4 (range 17,244 bp; 1,132-18,376 bp) sites (**Fig. 3k**). Finally, there were differences in chromosomal distribution of these transcripts, most notably when comparing the transcripts with n ≤ 2 vs. n > 2 m^6A sites (**Fig. 3l**). Given the use of glioma cell line, we also performed a functional (ontology) analysis of the detected sites stratified into the clusters described earlier (**Fig. 3e-g**).

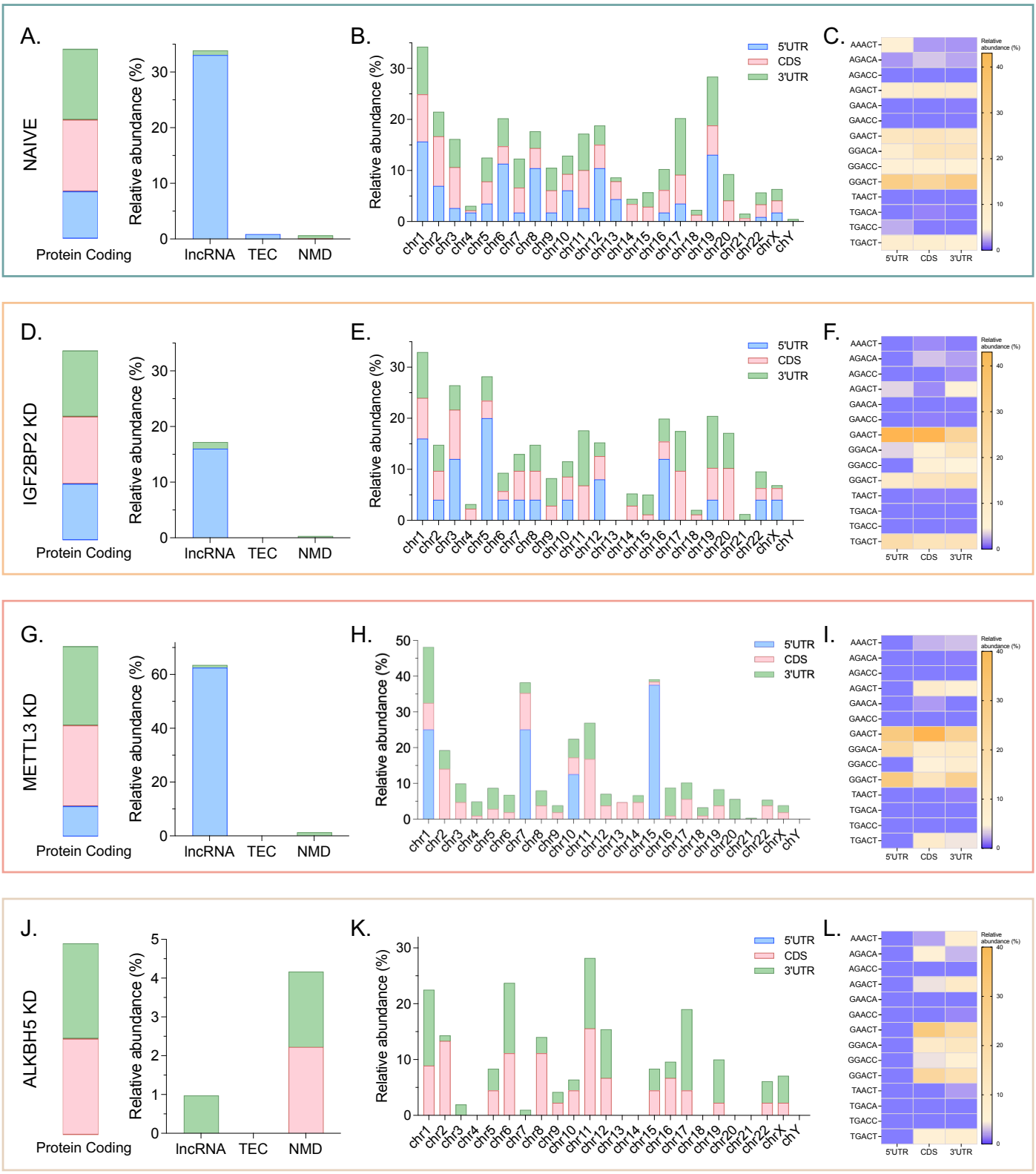

Figure 4. Transcriptome wide profiling of control and knockdown specific m^{6}A sites. *(a-l) The detected m^{6}A sites unique to the control (naive) and each knockdown (IGF2BP2 KD,*

METTL3 KD, ALKBH5 KD) condition analyzed further to identify patterns of transcriptome wide distribution. (a, d, g, j) Stacked plots comparing the relative distribution of detected protein coding (left) and non-protein coding (right) m^{6}A sites across the transcript regions (5'UTR, CDS, 3'UTR) in: (a) naive (control), (d) IGF2BP2 KD, (g) METTL3 KD, and (j) ALKBH5 KD derived RNA. (b, e, h, k) Stacked plots comparing the chromosomal distribution of detected m^{6}A sites across the transcript regions (5'UTR, CDS, 3'UTR) in: (b) naive (control), (e) IGF2BP2 KD, (h) METTL3 KD, and (k) ALKBH5 KD derived RNA. (c, f, i, l) Heatmaps demonstrating the variation in distribution of detected m^{6}A kmers across the transcript regions (5'UTR, CDS, 3'UTR) in: (c) naive (control), (f) IGF2BP2 KD, (i) METTL3 KD, and (l) ALKBH5 KD derived RNA.

Unique m^{6}A sites for each condition.

Across all conditions, m^{6}A sites in protein coding RNA were mostly localized to the CDS region followed by 3'UTR and 5'UTR regions (**Fig. 4a, d, g, j**). However, there were notable differences in the m^{6}A abundance in the 5'UTR region of protein coding RNA across the conditions. IGF2BP2 KD condition was shown to have higher (84%, **Fig. 4d**) m^{6}A abundance when compared to naive (66%, **Fig. 4a**). This is opposite to the lower 5'UTR m^{6}A abundance in METTL3 KD (37.5%, **Fig. 4g**) and no detection of m6A sites in the 5'UTR region of ALKBH5 KD RNA (**Fig. 4g**). In summary, compared to naive, lower m^{6}A abundance in the 5'UTR region of protein coding RNA was noted in the writer (**Fig. 4g**) and eraser (**Fig. 4j**) KD but higher in the reader KD (**Fig. 4d**). LncRNA biotype was shown to be almost exclusively modified in the 5'UTR region across all conditions (**Fig. 4a, d, g, j**). Furthermore, the highest prevalence of m^{6}A modified lncRNA in the 5'UTR region was noted in METTL3 KD (62.5%, **Fig. 4g**) condition followed by naive (33%, **Fig. 4a**) and IGF2BP2 KD (16%, **Fig. 4d**) conditions. Finally, nonsense mediated decay RNA (NMD RNA) was seen to be modified in both CDS (naive: 0.05%, ALKBH5 KD: 2.22%) and 3'UTR (naive: 0.58%, ALKBH5: 1.94%) regions of naive and ALKBH5 KD RNA, but only in the 3'UTR regions of IGF2BP2 and METTL3 KD conditions (**Fig. d, g, j**). Importantly, writer (METTL3, **Fig. 4g**) and eraser (ALKBH5, **Fig. 4j**) KD conditions demonstrated a higher prevalence of m^{6}A modified NMD (METTL3 KD; 1.31%, ALKBH5 KD; 1.94%) when compared to naive and reader KD (IGF2BP2, **Fig. 4d**) conditions.

Knockdown specific chromosomal (Chr) distributions of m^{6}A sites demonstrated further differences across the RNA transcript regions (**Fig. 4b, e, h, k**). In naive condition, m^{6}A sites demonstrated an approximately even distribution across the three regions with some peaks reflecting chromosomal enrichment: 5'UTR (Chr 1, 6, 8, 12, 19), CDS and 3'UTR (Chr 1, 2, 3, 11, 17) (**Fig. 4b**). IGF2BP2 KD RNA had notable peaks in the 5'UTR region (Chr 1, 3, 5, 16), 3'UTR region (Chr 1, 11, 19), and CDS region (Chr 1, 3, 17, 20) (**Fig. 4e**). METTL3 KD condition demonstrated enrichment in 5'UTR region (Chr 1, 7, 10, 15), 3'UTR region (Chr 1, 11), and CDS region (Chr 2, 7, 11) (**Fig. 4h**). ALKBH5 KD RNA demonstrated enrichment in 3'UTR region (Chr 1, 6, 11, 17), and CDS region (Chr 1, 2, 6, 8, 11) (**Fig. 4k**). When comparing conditions, the 3'UTR region was consistently modified in Chr 1 and 11 across all conditions, with higher enrichment noted in Chr 1 of METTL3

KD (15.7%, **Fig. 4h**) and ALKBH5 KD RNA (13.6%, **Fig. 4k**) vs. naive (9.4%, **Fig. 4b**). Specific to IGF2BP2 KD condition, a peak was noted in Chr 19 (10.2%, **Fig. 4e**). Similar to 3'UTR, CDS region was also seen to be consistently modified in Chr 1 and 2 in all conditions, with higher enrichment noted in Chr 2 of METTL3 KD (14.0%, **Fig. 4h**) and ALKBH5 KD RNA (13.3%, **Fig. 4k**) vs. naive (9.7%, **Fig. 4b**). Both METTL3 KD (16.8%, **Fig. 4h**) and ALKBH5 KD (15.6%, **Fig. 4k**) also demonstrated higher enrichment in Chr 11 when compared to naive (7.4%, **Fig. 4b**). While both CDS and 3'UTR demonstrated unique enrichment patterns in METTL3 KD and LAKBH5 KD RNA, no 5'UTR sites were seen in the latter (**Fig. 4k**). Similar to 3'UTR and CDS, 5'UTR was consistently modified in Chr 1 of the remaining three conditions with higher (25%) abundance in METTL3 KD RNA (**Fig. 4h**). Interestingly, 5'UTR region in Chr 6 was uniquely enriched in naive (11.3%, **Fig. 4b**) and IGF2BP2 KD (4%, **Fig. 4e**) with no sites in METTL3 KD and ALKBH5 KD RNA. In short, IGF2BP2 KD had notable peaks in 5'UTR (Chr 3, 5, 16), CDS (Chr 17, 20) and 3'UTR modifications (Chr 1). METTL3 KD highlighted strong enrichment in 5'UTR (Chr 1, 15), CDS (Chr 2, 7, 11), and 3'UTR (Chr 1, 16) regions. ALKBH5 KD RNA demonstrated moderate levels in CDS (Chr 2, 6, 8, 11), and 3'UTR (Chr 1, 6, 12) regions.

Finally, we also observed regional specific differences in distribution of m^6A Kmers across the four conditions (**Fig. 4c, f, i, l**). AAACT was highly enriched in the 5'UTR region of naive RNA (7.0%, **Fig 4c**) but was not detected in the 5'UTR region of any KD conditions. CDS enrichment was consistent across the conditions, but compared to the naive 3'UTR region (1.64%, **Fig. 4c**), the abundance was remarkably lower in IGF2BP2 KD (0.30%, **Fig. 4f**) and higher in METTL3 KD (3.26%, **Fig. 4i**) and ALKBH5 KD RNA (8.74%, **Fig. 4l**). A similar change was also observed for AGACA and AGACT, with loss of 5'UTR enrichment in KD conditions (**Fig. 4c, f, i, l**). However, almost a 2-fold higher enrichment of AGACA in the CDS region was noted in ALKBH5 KD condition (**Fig. 4l**). For AGACT, a reduction in the enrichment in the CDS region was also seen in IGF2BP2 KD and ALKBH5 KD conditions. TGACT was seen to be uniquely enriched in IGF2BP2 KD RNA across all three regions with loss of detection in 5'UTR regions of METTL3 KD and ALKBH5 KD RNA. Overall, naive RNA exhibited a broad distribution of several kmers, with a notable high presence of AGACA (5'UTR), AGACT (5'UTR, CDS, 3'UTR), AAACT (5'UTR), GGACA (CDS), and GGACC (5'UTR) (**Fig. 4c)**. IGF2BP2 KD RNA was enriched in GAACT and TGACT motifs (5'UTR, CDS, 3'UTR) (**Fig. 4f)**. METTL3 KD RNA was enriched in GAACT (5'UTR, CDS, 3'UTR), GAACA (CDS), and GGACA (5'UTR) motifs (**Fig. 4i)**. Finally, ALKBH5 KD RNA demonstrated higher enrichment of TAACT (3'UTR), GAACT (CDS, 3'UTR), and AGACA (CDS) (**Fig. 4l**).

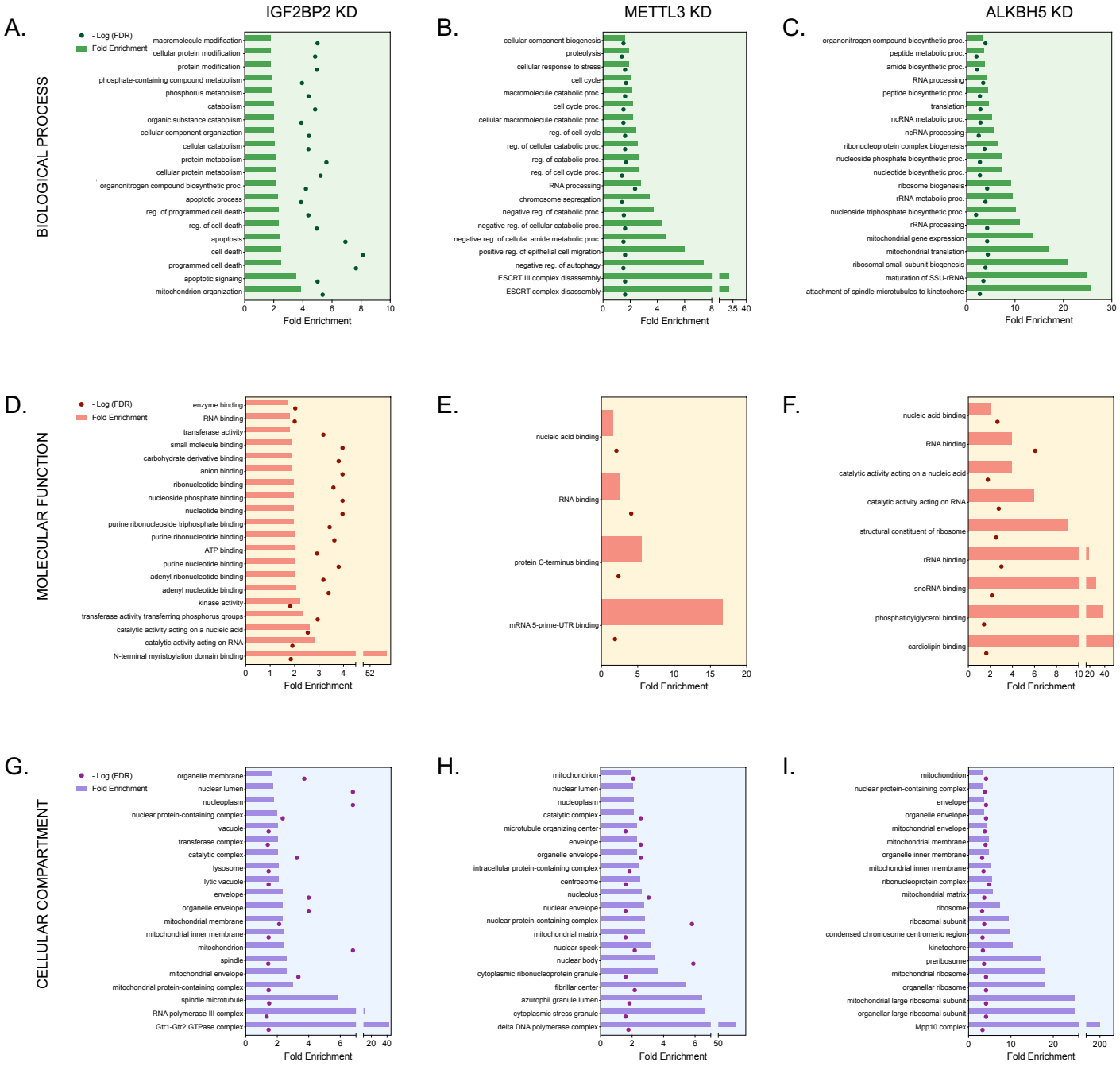

Figure 5. Functional ontology analysis of knockdown specific m^{6}A sites. *(a-i) Gene ontology (GO) analysis of the unique m^{6}A sites in each knockdown (IGF2BP2 KD, METTL3 KD, ALKBH5 KD) condition using ShinyGO. Bar-graphs plotting fold enrichment and –Log (FDR) of the enriched pathways in: (a-c) biological process, (d-f) molecular function, (g-i) cellular compartment.*

Mapping Functional Ontologies.

Functional consequences of m^6A sites unique to each knockdown condition were identified by performing ontology analysis in three categories: biological process (**Fig. 5a-c**), molecular function (**Fig. 5d-f**), and cellular compartment (**Fig. 5g-i**).

Enriched biological processes in IGF2BP2 KD include cellular protein modification, phosphate-containing compound metabolism, protein metabolism, regulation of programmed cell death and apoptosis, and mitochondrion organization (**Fig. 5a)**. METTL3 KD RNA demonstrated strong enrichment in cellular component biogenesis, regulation of cell cycle and response to stress, RNA processing, and cellular macromolecule biosynthesis, linking METTL3 to transcriptional and translational control. Importantly, enrichment of ESCRT complex disassembly highlights a potential role in membrane repair and exosome biogenesis (**Fig. 5b)**. RNA processing, metabolism, and translation related processes were significantly enriched in ALKBH5 KD condition (**Fig. 5c)**. Ribosome biogenesis, ribonucleoprotein complex assembly, peptide metabolism, and rRNA metabolism signify a link to protein synthesis machinery. We also noted enrichment of terms relating to ncRNA processing and metabolism (**Fig. 5c)**.

Molecular functions enriched in IGF2BP2 KD condition involve enzyme binding, RNA binding, ribonucleotide binding, nucleoside triphosphate binding, and catalytic activity, suggesting that IGF2BP2 affects multiple enzymatic pathways and RNA interactions. Significant enrichment of N-terminal myristoylation domain binding indicates a potential role in lipid metabolism and cellular signaling (**Fig. 5d)**. Consistent with previous observation of a potential role in RNA processing, METTL3 KD was particularly enriched in molecular functions regulating mRNA 5'UTR binding, protein C terminus binding, and RNA binding (**Fig. 5e)**. Finally, molecular roles highlighting translation were significantly enriched in ALKBH5 KD: catalytic activity, rRNA/snoRNA/ binding, cardiolipin binding, and structural constituent of ribosome (**Fig. 5f)**.

Cellular compartments significantly enriched in IGF2BP2 KD condition closely reflected the processes highlighted above: cell death and apoptosis (lytic vacuole, lysosomes), mitochondrion organization (mitochondrial envelope, inner membrane), protein modification (RNA polymerase III complex, nuclear lumen), response to cell stress (Gtr1-Gtr2 GTPase complex) (**Fig. 5g)**. A wider intracellular distribution was noted for METTL3 KD with enrichment in stress granules, cytoplasm (mitochondria, microtubule organizing center), nucleus, and DNA polymerase complex (**Fig. 5h)**. Finally, significant enrichment was seen in translational machinery for ALKBH5 condition: ribosomal subunits, pre ribosome, mitochondrial and organelle ribosome, Mpp 10 complex (**Fig. 5i)**.

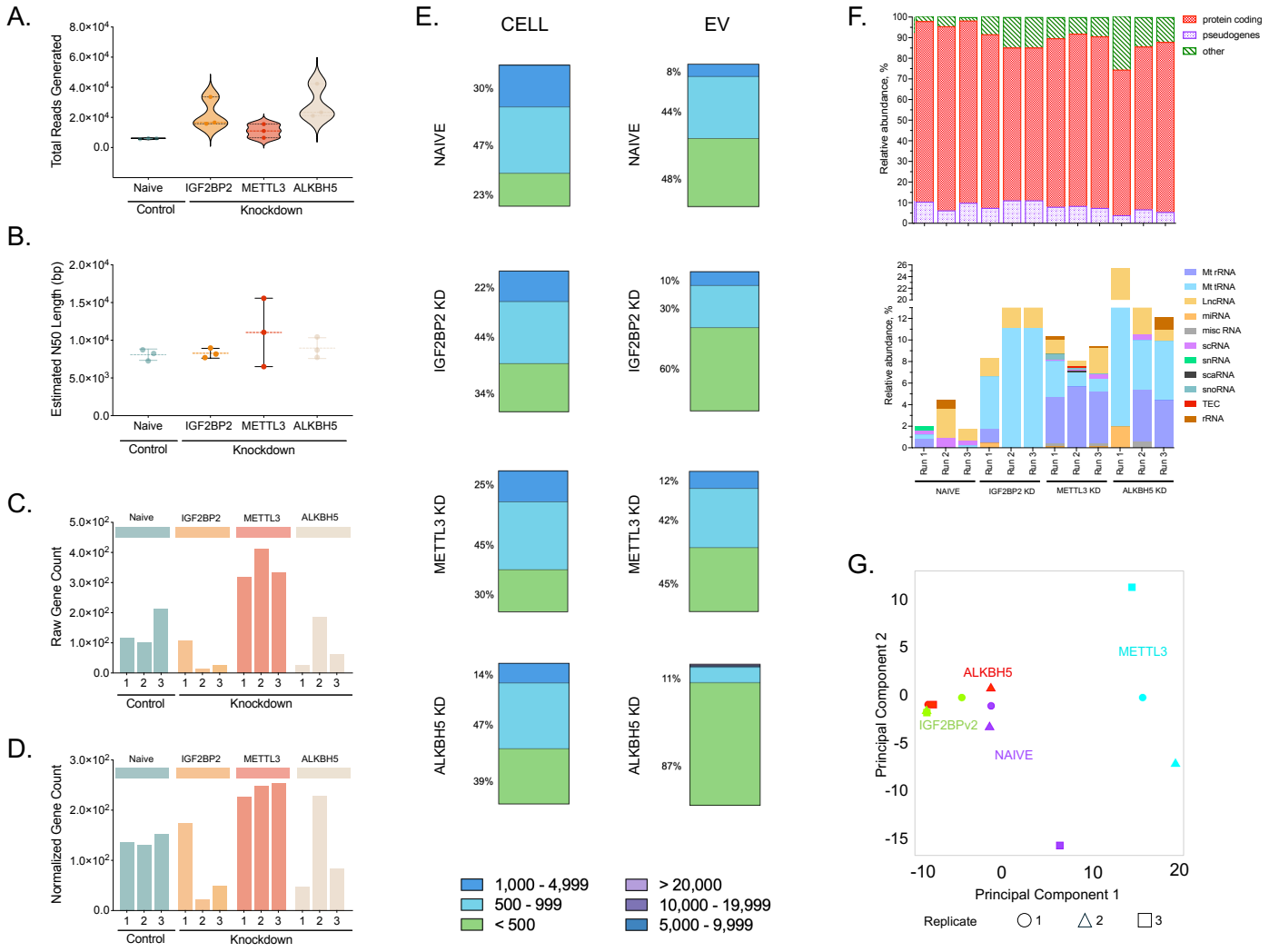

Figure 6. Extracellular vesicle (EV) direct RNA sequencing approach. *(a-b) Extracellular vesicle (EV) RNA isolated from control and KD cells sequenced using Nanopore direct RNA sequencing platform. Three technical replicates sequenced per condition. (a) Total reads generated and (b) N50 read length summarized for the three replicates per condition. Bar-graphs depicting (c) total and (d) normalized (variance-stabilizing transformation, VST) gene counts detected across the three replicates in control and KD conditions. (e) Stacked plots comparing the prevalence (%) of full-length RNA transcripts of varying lengths (<500bp - >20,000bp) in Cell vs. EV RNA sequenced from control and KD conditions. (f) Stacked bar graphs demonstrating the relative abundance of the EV RNA biotypes across the n = 4 conditions. (g) Assessment of variance in the EV RNA detected transcripts using principal*

component analysis (PCA).

Identification of full length transcripts in EV RNA.

Preliminary analysis of the sequencing output from EVs demonstrated a similar distribution of reads generated in naive vs. knockdown conditions (**Fig. 6a**). Similarly, the N50 (median) read length was not different across the four conditions (**Fig. 6b**). Gene count before (**Fig. 6c**) and after (**Fig. 6d**) normalization did not significantly alter in distribution across the individual replicates. Overall, more variability was observed in IGF2BP2 KD and ALKBH5 KD EVs vs naive and METTL3 KD conditions (**Fig. 6d**).

Nanopore RNA sequencing platform offers a unique opportunity for full-length RNA transcripts discovery and quantification. We explored full-length transcripts across different conditions in both cells (**Fig. 6e, left**) and EVs (**Fig. 6e, right**) using Bambu[17]. Interestingly, there were no significant changes in the distribution of cell derived full-length RNA transcripts across different knockdown conditions (**Fig. 6e, left**). However, in ALKBH5 KD EVs there was a remarkable increase in the proportion of short (< 500 bp) RNA transcripts when compared to other conditions. On the other hand METTL3 KD EVs had the least proportion of short (< 500 bp) RNA transcripts. Furthermore, out of all knockdown conditions, METTL3 KD EVs also had the highest prevalence of longer (500-999 bp) RNA transcripts (**Fig. 6e, right**).

Relative abundance of the RNA biotypes demonstrated more variability in the prevalence of protein coding EV RNA (**Fig. 6f**) across naive and knockdown conditions vs. cells (**Fig. 6e**). Naive EV RNA had the highest prevalence of protein coding RNA whereas the lowest prevalence was noted in ALKBH5 KD (**Fig. 6f, top**). In the non-protein coding biotypes (**Fig. 6f, bottom**), we noted a higher prevalence of mitochondrial RNA in IGF2BP2 KD and ALKBH5 KD EV RNA vs. METTL3 KD and naive conditions (**Fig. 6f, bottom**). Importantly, similar biotype distribution was also described earlier in cell RNA (**Fig. 6e**). Finally, we also observed a higher prevalence of LncRNA in ALKBH5 KD EVs (**Fig. 6f, bottom**).

Results from principal component analysis (PCA) (**Fig. 6g**) demonstrated an overall 50.9% total variance in the data, with PC1 accounting for 37.7% of the variance, and PC2 contributing 13.2% (**Fig. 6g**).

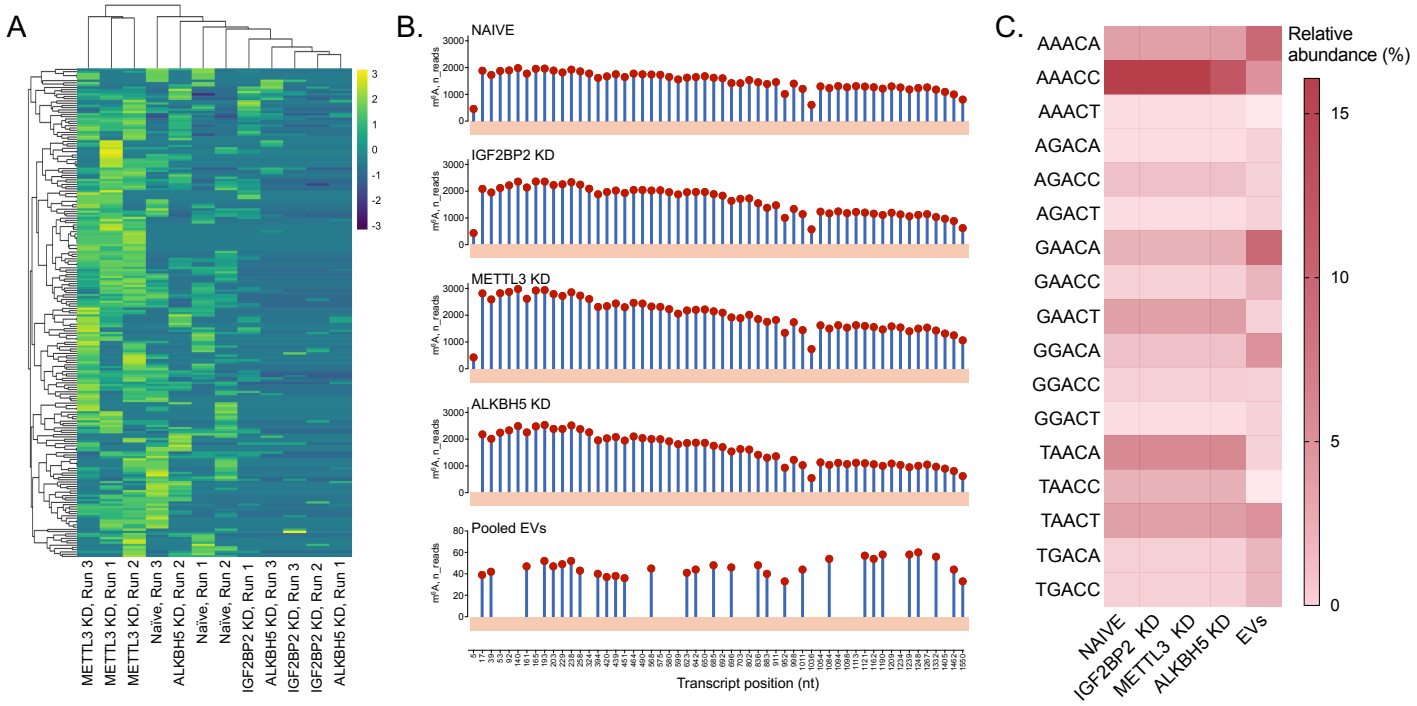

Figure 7. Extracellular vesicle (EV) m^{6}A RNA detection. *(a) Heatmap depicting clustering analysis of the detected transcripts demonstrating change in expression patterns across the control and knockdown conditions. (b) Dot-plots demonstrating the location (x-axis, transcript position) and prevalence (y-axis, n_reads) of detected m^{6}A sites in the MT-RNR2-201 isoform spanning 1,559 bp in length. m^{6}A sites mapped in RNA derived from cells (KD, control) and pooled EVs. (c) Heatmap comparing the relative abundance (%) of detected m^{6}A kmers (MT-RNR-201) in cells vs. EVs.*

m^{6}A sites in EV RNA.

Variance stabilizing transformation (VST) was performed to normalize the transcript counts across the naive and knockdown conditions (**Fig. 7a**). Overall, naive and METTL3 KD EV RNA clustered together. On the other hand, ALKBH5 and IGF2BP2 KD EV RNA expression was seen to be more similar (**Fig. 7a**). Using m6Anet we aimed to detect m^{6}A sites in EV RNA. However, the reads from individual sites did not qualify the cut-offs to be considered for probability estimation. Subsequently, all EV reads were pooled and we were able to detect 30 m^{6}A sites in the MT-RNR2-201 isoform (**Fig. 7b**). Importantly, the predicted probability of modification was below 0.9. Comparing the results to cells, we identified m^{6}A sites in MT-RNR2-201 across the control and three knockdown

conditions (probability of modification < 0.9). For each condition we detected approximately 50 different positions along the length of the isoform (1,559 bp). In addition to the presence of the m^6A site we also quantified the differences in modified reads at each site (**Fig. 7b**). While the location of modification was similar we did observe higher counts in cells vs. EVs. Furthermore, across the cells, the highest number of reads were noted in METTL3 KD condition (**Fig. 7b**). Finally, we also quantified the distribution of the m^6A Kmers in cells and EVs (**Fig. 7c**). There were no significant differences in the relative abundance of kmers across the naive and KD cell conditions. However, in the pooled EVs we did observe a higher abundance of AAACA, GAACA, and GGACA motifs when compared to cells (**Fig. 7c**).

Discussion

In this study, we investigated the impact of modulating m^6A regulatory machinery on the m^6A landscape of a glioma cell line through a targeted knockdown (KD) of: IGF2BP2 (reader), METTL3 (writer), and ALKBH5 (eraser). The results highlight common and unique functional consequences of the RNA methylation profiles, providing important insights into the glioma biology.

Consistent with previous findings, we also report a conservation of the DRACH m^6A motif (GGACT) across all the KD conditions and naive control[18,19]. Transcriptome wide distribution of m^6A modifications demonstrated an overall enrichment in 3'UTR and CDS regions. However, we also observed differential enrichment patterns of secondary motifs such as AAACT, AGACT, and TGACT. The variability was found to be secondary to not only the KD condition but also the transcript region. For instance, both IGF2BP2 and METTL3 KD RNA demonstrated a higher enrichment of GAACT (5'UTR, CDS, 3'UTR). In contrast, there was a reduction in the abundance of 5'UTR sites of GAACT in ALKBH5 KD condition. Interestingly, we observed a total loss of 5'UTR specific m^6A sites with the KD of ALKBH5. This effect was also seen in the DRACH, GGACT motif with similar CDS enrichment but lower 3'UTR and absent 5'UTR enrichment when compared to naive.

We quantified detected m^6A sites, transcripts, and genes. Highest percentage of modified sites was seen in naive and lowest in ALKBH5 KD condition. This was also true for modified transcripts and genes. Interestingly, IGF2BP2 and METTL3 KD conditions had similar prevalence of m^6A sites, both higher than ALKBH5 KD RNA. Analysis of the biotype distribution across the m^6A transcripts did not demonstrate any differences unique to the knockdown. Across all conditions, protein coding RNA was most likely to be modified followed by nonsense mediated decay RNA and retained intron RNA. Multi-region (5'UTR, CDS, 3'UTR) methylated transcripts were more likely to be found in naive versus KD RNA.

Our analysis included investigation of both common and unique m^6A sites. Overall, 716 sites were commonly modified in control and KD conditions. Since the RNA was isolated from the glioma cell

line, we further performed an enrichment and functional analysis of the 716 sites. Interestingly, by utilizing a cut-off of log2 reads > 5.9 reads, we were able to isolate two distinct clusters: 357 sites present in all knockdown conditions and 338 sites detected only in IGF2BP2 KD and METTL3 KD conditions. Ontology analysis of the three groups 9716, 357, 338 sites) highlighted differences in enrichment of biological processes and molecular function. Overall, most of the genes had only 1 modified isoform. Interestingly, EEF1A1 had 15 m^6A modified isoforms. At the isoform level, the number of sites per isoform ranged from 1 to 4. There was no significant difference in the overall transcript length between isoforms having 1 versus > 1 m^6A sites per isoform.

Following analysis of the common 716 sites, we looked at the m^6A sites unique to each condition. Consistent with previous observations, naive RNA had the highest number of unique sites with the lowest number seen in ALKBH5 KD RNA. Across all comparisons (control, KD) we noticed that while protein coding RNA was likely to be modified in all three transcript regions, lncRNA was mostly modified in the 5'UTR region. Interestingly, no m^6A sites unique to the ALKBH5 KD RNA were localized to the 5'UTR region. Furthermore, a higher prevalence of modified NMD RNA was observed in the ALKBH5 KD RNA (CDS, 3'UTR). Knockdown specific chromosomal (Chr) distributions of m^6A sites demonstrated further differences across the RNA transcript regions**.** Both IGF2BP2 KD and METTL3 KD conditions had notable transcriptome wide (5'UTR, CDS, 3'UTR) peaks in Chr 1 and 16. ALKBH5 KD RNA demonstrated moderate levels in CDS (Chr 2, 6, 8, 11), and 3'UTR (Chr 1, 6, 12) regions.

Functional analysis of the KD specific unique sites highlighted distinct biological pathways. For IGF2BP2 KD the enriched terms include cellular protein modification, phosphate-containing compound metabolism, protein metabolism, regulation of programmed cell death and apoptosis, and mitochondrion organization. METTL3 KD RNA demonstrated strong enrichment in regulation of cell cycle and response to stress, and RNA processing. Finally, ALKBH5 KD RNA was linked to ribosome biogenesis, ribonucleoprotein complex assembly, peptide metabolism, and protein synthesis. Hallmark pathways enriched in each KD condition were consistent with these findings: IGF2BP2 KD (reactive oxygen species, oxidative phosphorylation), METTL3 KD (unfolded protein response, E2F targets), ALKBH5 KD (MYC targets V1, MYC targets V2, DNA repair).

This is the first study reporting full-length RNA transcripts in EVs using long-read, direct RNAseq. As expected, we did see a high proportion of <500 bp transcripts, but there was also detection of transcripts longer than 500 bp (up to 5,000bp). Interestingly, the distribution of the transcripts varied across the KD conditions. ALKBH5 KD EV RNA was more likely to be degraded with a higher proportion of transcripts, <500 bp. In contrast, METTL3 KD EV RNA had the highest prevalence of longer (500-999 bp) transcripts and least proportion of transcripts, < 500bp. By pooling the EVs we were also able to detect m^6A sites in MT-RNR2-201 isoform, albeit with a probability < 0.9. Importantly, this isoform spans 1,559 bp and was seen to be modified at 30 distinct sites. Furthermore, we also noted a significant overlap of the m^6A sites in MT-RNR2-201 detected in cell

derived RNA (control and KD) conditions. All the 30 m^6A sites detected in pooled EVs were also detected in the cells.

In conclusion, our study provides a comprehensive overview of how modulating key m6A regulators (reader, writer, and eraser) alters the m^6A RNA methylation landscape in glioma cells. We report important findings contributing to the understanding of m^6A modifications at the transcript and site level. Our analysis of common and unique m^6A sites revealed enrichment in distinct biological pathways and hallmark processes, elucidating the critical role of m^6A modifications in glioma biology. Future work involving larger samples and multiple cell lines will further advance our understanding of how m^6A machinery regulates gene expression in low- and high-grade gliomas. Finally, our preliminary findings from EV analysis highlights the importance of studying m^6A in both intra- and extra- cellular space. Such future studies can identify novel diagnostic, prognostic, and therapeutic EV m^6A RNA biomarkers.

Methods

Study Population

Human glioma cell line expressing mutant epidermal growth factor receptor, variant III ($Gli36^{EGFRvIII}$; generated at Massachusetts General Hospital with approved IRB procedures) was utilized for *in vivo* m^6A RNA methylome profiling. Knockdown (KD) of three distinct m^6A regulators was achieved by silencer RNA (siRNA) mediated transfection. A total of n = 4 experimental conditions were tested: (i) naive, no treatment, (ii) ALKBH5 (eraser) KD, (iii) IGF2BP2 (reader) KD, and (iv) METTL3 (eraser) KD. For each condition, both cellular (n = 4 conditions) and extracellular vesicle (EV) RNA (n = 4 conditions) were sequenced. Three technical replicates were performed per sample, yielding a total of N = 24 sequencing runs.

Selected Silencer RNA (siRNA) for m^6A regulator knockdown

Select Pre-designed siRNAs (Catalog Number: 4427037) were purchased from ThermoFisher Scientific for knockdown of known m6A regulators: ALKBH5 (siRNA ID: s29688), IGF2BP2 (siRNA ID: s20924), and METTL3 (siRNA ID: s32142).

Cell line transfection and collection

On Day 0 (one day before transfection), 2 x 10^5 $Gli36^{EGFRvIII}$ cells were plated in a 6-well plate using Opti-MEM™ reduced serum medium (ThermoFisher Scientific, Waltham, MA, USA). The following day, cells were checked to ensure 60-80% confluency prior to transfection. Transfection on Day 1 was performed using Lipofectamine RNAiMAX Reagent (ThermoFisher Scientific, Waltham, MA, USA) according to manufacturer's instructions. Briefly, both lipofectamine RNAiMAX reagent and silencer RNA (siRNA) concentrates were diluted in Opti-MEM medium. A volume of 3 µl of 10 µM siRNA was combined with 150 µl of Opti-MEM medium to achieve a final concentration of 30 pmol. RNA-lipid complexes were then prepared by combining diluted siRNA and diluted lipofectamine RNAiMAX reagent in a 1:1 ratio followed by 5 min incubation at room temperature. The siRNA-lipid

complex was then added to the individual wells of the 6 well plate. The reaction mixture was mixed gently by rocking the plate back and forth. Cells were transfected for 48h at 37℃ in a CO_2 incubator to achieve optimal m^6A regulator knockdown. On Day 3, the Opti-MEM medium was carefully aspirated and replaced with Dulbecco's Modified Eagle Medium (DMEM, Invitrogen, Waltham, MA) with high glucose containing 10% fetal bovine serum (FBS; Life Technologies Corporation, Carlsbad, CA, USA) and 1% Penicillin/Streptomycin solution (Pen/Strep; Life Technologies Corporation, Carlsbad, CA, USA). Transfected cells were cultured in DMEM for 24h and transferred to T-75 flask on Day 4. On Day 7, cells were transferred to Nunc™ TripleFlask™ Treated Cell Culture Flasks for cell culture expansion. On Day 8, the media was replaced with EV-free media: DMEM, containing 3% EV-depleted fetal bovine serum (EV-free FBS; Life Technologies Corporation, Carlsbad, CA, USA) and 1% Pen/Strep. On Day 9, conditioned media was collected for downstream processing and analysis. Cell viability and number was assessed using the Countess II FL Automated Cell Counter (ThermoFisher Scientific, Waltham, MA, USA). For downstream analytics, cells were pelleted to create multiple aliquots (3×10^6 cells per aliquot) and stored at -80°C until further analysis.

Conditioned Media processing

The media collected from transfected cells was centrifuged at 300 × g for 5 min at room temperature (RT) to remove floating cells. The supernatant was collected and centrifuged again at 2000 × g for 20 min at RT and filtered using a 0.8 µm filter to remove cellular debris and other aggregates. The media was stored in amber tubes (50 ml aliquots) at −80°C until further analysis.

Mycoplasma Contamination testing

Testing for mycoplasma contamination was performed using a commercial mycoplasma PCR kit (PCR Mycoplasma Detection kit; Applied Biological Materials Incorporated, BC, Canada). The testing was done at two stages of the workflow: (i) Day 3, end of 48h transfection period, and (ii) Day 7, prior to transfer of cells from T-75 flask to Nunc™ TripleFlask™.

Assessment of transfection efficiency

Quantification (percentage gene knockdown) and stability of transfection were assessed using quantitative polymerase chain reaction (qPCR) measurement of the target. To ensure stability of transfection, quantification was performed using cells collected from three stages of the workflow: (i) 6 well plate, (ii) T-75 flask, and (iii) Nunc™ TripleFlask™. Commercially available, pre-designed TaqMan gene expression assays were purchased (ThermoFisher Scientific, Waltham, MA, USA) for ALKBH5, IGF2BP2, and METTL3. Isolated total RNA from transfected (KD, control) cells was reverse transcribed using SuperScript™ VILO™ cDNA Synthesis Kit (ThermoFisher Scientific, Waltham, MA, USA). The qPCR reaction was performed in the Applied Biosystems StepOnePlus Real-Time PCR (Thermo Fisher Scientific) in a final volume of 20 µl and was prepared using 10 µl of TaqMan Universal Master Mix II, no UNG (Thermo Fisher Scientific), 1 µl of 20X gene expression assay, and cDNA. Each sample was run in three replicates. The data was analyzed by visualizing amplification plots and comparing the Cycle threshold (C_t) values in knockdown (ALKBH5,

IGF2BP2, METTL3) and control (scrambled siRNA) wells. Normalization was performed using GAPDH as a reference assay (ThermoFisher Scientific).

Cellular RNA Extraction and Quantification

Total RNA was extracted from transfected cells using TRIzol lysis reagent (ThermoFisher Scientific, Waltham, MA, USA) per manufacturer's protocol. For each condition, 3 x 10^6 million cells were lysed using 3 ml TRIzol. The extracted RNA was then eluted in xx µl of nuclease free water (Qiagen). Agilent RNA 6000 Pico Kit was used with Agilent Technologies 2100 Bioanalyzer to determine the concentration and RIN (RNA Integrity Number) value of the samples. Isolated RNA was stored at −80°C prior to downstream analysis.

Extracellular Vesicle (EV) RNA Isolation and Quantification

For each transfection condition, 50 ml conditioned media was used for EV RNA isolation. EV RNA was isolated using the ExoRNeasy Maxi Kit (Qiagen), per the manufacturer's recommendations. Following concentration and wash steps. EV RNA was eluted in 17 µL of nuclease-free water (Qiagen) and assessed for concentration and purity with Bioanalyzer Agilent RNA 6000 Pico Kit.

Cellular and EV messenger RNA (mRNA) enrichment

Following Cell RNA and EV RNA extraction, total RNA was selectively enriched for mRNA using RiboMinus™ Eukaryote Kit v2 (ThermoFisher Scientific, Waltham, MA, USA) per manufacturer's recommendations. This provides transcriptome isolation downstream sequencing by selectively depleting 5S, 5.8S, 18S, and 28S ribosomal RNA from total RNA. For high yield cell RNA, RiboMinus™ Eukaryote Kit v2 (Catalogo ID: A15026) and for low yield EV RNA, Low Input RiboMinus™ Eukaryote System v2 (Catalogo ID: A15027) was used to maximize the mRNA enrichment and overall recovery.

RNA Quality Control Steps

Different measures were integrated throughout the workflow for quantitative and qualitative analysis of cell RNA and EV RNA. Quantification of "isolated total RNA" and "mRNA post rRNA depletion" was performed using Bioanalyzer Agilent RNA 6000 Pico Kit. Overnight ethanol precipitation with 3M sodium acetate at −20°C was performed post RNA extraction and post rRNA depletion to prevent carry over inhibitors during library preparation.

Library Preparation and Sequencing

Direct RNA sequencing of Cell and EV derived mRNA was performed using the Oxford Nanopore technologies (ONT) platforms. Libraries were prepared using SQK-RNA002 (ONT) kit per manufacturer's protocol. The library was then sequenced on the MinION software using flow cells 9.4.1 (FLO-MIN106D, ONT). No multiplexing was done and each sample was run individually for (24-72)h.

Data Analysis

Preprocessing

Raw RNA sequencing reads from cell and EVs generated using ONT were and basecalled from POD5 files using Dorado (v0.5). Basecalling was performed with default settings, utilizing the decoder file “rna002_70bps_fast@v3” to convert raw nanopore signal data into FASTQ format, optimized for RNA sequencing at 70 base pairs per second. All reads that passed the default basecallign quality filters in Dorado were retained for downstream analysis.

The basecalled reads were then aligned to the human transcriptome (GENCODE v45, GRCh38) using minimap2 (v2.26). All passing aligned reads were included in the analysis. The BAM files were sorted and indexed using Samtools (v1.19). The processed and indexed BAM files were then used for transcript quantification and subsequent analyses.

Quantification

Transcript quantification was performed using bambu (v3.4.1), which supports the quantification of both known and novel transcripts, as well as full length transcripts from long-read RNA sequencing data. BAM files generated by minimap2 were used as input along with the GENCODE v45GRCh38 genome and annotation files. Transcript expression levels were quantified for each sample, with both raw counts and transcript per million (TPM) values calculated. Bambu was configured to detect novel transcript isoforms in addition to quantifying known transcripts. To ensure robust quantification, transcripts with zero counts were were excluded from analysis in the Cell RNA data, and transcripts with zero counts in more than two samples across all experimental conditions were excluded from the analysis in the EV RNA data.This filtering step reduced the noise and ensured that low-abundance transcripts did not affect downstream analyses.

Differential Expression Analysis

To assess differential transcript expression between the control (Naive) and knockdown conditions (IGF2BP2, METTL3, ALKBH5 knockdowns transcript-level counts were analyzed using DEseq2 (v1.42.1). For Cell RNA data, transcripts counts generated by bambu were imported into DESeq2, where normalization was performed using variance-stabilizing transformation (VST) in the Cell RNA data. For the EV RNA data, due to the low abundance of transcript counts, raw transcript counts were normalized using R (v4.3.2). This involved calculating the geometric mean of each transcript across samples, followed by the median of ratios, which accounts for differences in sequencing depth. This method follows the normalization strategy described in DESeq2, to ensure that library size differences and low read counts in the EV RNA data were appropriately accounted for.

After normalization, differential expression analysis was performed to identify transcripts with significant changes in expression between the control and knockdown conditions. Transcripts with an absolute log2 fold change greater than 2 and an adjusted p-value (Benjamini-Hochberg) less than 0.05 were considered significantly differentially expressed.

RNA Methylation Analysis

RNA methylation analysis was conducted using m6anet (v2.1.0) to detect RNA modifications at single-nucleotide resolution. BAM files obtained from minimap2 were input to m6anet, along with the raw FAST5 files, FASTQ, and transcriptome files. The model was trained using the RNA004 direct RNA-Seq run using HEK293T cell line. Sites with a probability of modification greater than 0.9 were considered high confidence m6a sites and retained for downstream analysis. The distribution of methylation sites was compared between control and knockdown conditions to investigate the impact of m6a regulators on RNA methylation patterns in glioma. Furthermore, we integrated the methylation data with differential expression results to explore the relationship between m6a modification and changes in transcript expression, particularly focusing on transcripts that exhibited both significant fold changes and altered m6a site patterns.

References

1. Akhtar, J., Lugoboni, M. & Junion, G. mA RNA modification in transcription regulation. *Transcription* **12**, 266–276 (2021).
2. Arzumanian, V. A., Dolgalev, G. V., Kurbatov, I. Y., Kiseleva, O. I. & Poverennaya, E. V. Epitranscriptome: Review of Top 25 Most-Studied RNA Modifications. *Int. J. Mol. Sci.* **23**, (2022).
3. Jiang, X. *et al.* The role of m6A modification in the biological functions and diseases. *Signal Transduct Target Ther* **6**, 74 (2021).
4. Huang, W. *et al.* N6-methyladenosine methyltransferases: functions, regulation, and clinical potential. *J. Hematol. Oncol.* **14**, 117 (2021).
5. Jiang, L., Li, X., Wang, S., Yuan, Z. & Cheng, J. The role and regulatory mechanism of mA methylation in the nervous system. *Front. Genet.* **13**, 962774 (2022).
6. Fan, Y., Lv, X., Chen, Z., Peng, Y. & Zhang, M. m6A methylation: Critical roles in aging and neurological diseases. *Front Mol Neurosci* **16**, 1102147 (2023).
7. Louis, D. N. *et al.* The 2021 WHO Classification of Tumors of the Central Nervous System: a summary. *Neuro Oncol* **23**, 1231–1251 (2021).
8. Xu, S., Tang, L., Li, X., Fan, F. & Liu, Z. Immunotherapy for glioma: Current management and future application. *Cancer Lett* **476**, 1–12 (2020).
9. Mohammed, S., Dinesan, M. & Ajayakumar, T. Survival and quality of life analysis in glioblastoma multiforme with adjuvant chemoradiotherapy: a retrospective study. *Rep Pract Oncol Radiother* **27**, 1026–1036 (2022).

10. Chen, J.-J. *et al.* The m6A reader HNRNPC promotes glioma progression by enhancing the stability of IRAK1 mRNA through the MAPK pathway. *Cell Death Dis* **15**, 390 (2024).
11. Zhang, Y. *et al.* m6A modification in RNA: biogenesis, functions and roles in gliomas. *J Exp Clin Cancer Res* **39**, 192 (2020).
12. Suvà, M. L. *et al.* Reconstructing and reprogramming the tumor-propagating potential of glioblastoma stem-like cells. *Cell* **157**, 580–594 (2014).
13. Yuan, F. *et al.* Roles of the mA Modification of RNA in the Glioblastoma Microenvironment as Revealed by Single-Cell Analyses. *Front Immunol* **13**, 798583 (2022).
14. Cui, Q. *et al.* mA RNA Methylation Regulates the Self-Renewal and Tumorigenesis of Glioblastoma Stem Cells. *Cell Rep* **18**, 2622–2634 (2017).
15. Batool, S. M. *et al.* Highly Sensitive EGFRvIII Detection in Circulating Extracellular Vesicle RNA of Glioma Patients. *Clin Cancer Res* **28**, 4070–4082 (2022).
16. Choi, B. D. *et al.* Intraventricular CARv3-TEAM-E T Cells in Recurrent Glioblastoma. *N Engl J Med* **390**, 1290–1298 (2024).
17. Chen, Y. *et al.* Context-aware transcript quantification from long-read RNA-seq data with Bambu. *Nat. Methods* **20**, 1187–1195 (2023).
18. Wang, K., Peng, J. & Yi, C. The mA Consensus Motif Provides a Paradigm of Epitranscriptomic Studies. *Biochemistry* **60**, 3410–3412 (2021).
19. Lorenz, D. A., Sathe, S., Einstein, J. M. & Yeo, G. W. Direct RNA sequencing enables mA detection in endogenous transcript isoforms at base-specific resolution. *RNA* **26**, 19–28 (2020).